How to cite: *Angew. Chem. Int. Ed.* **2023**, *62*, e202217476
doi.org/10.1002/anie.202217476

Li Metal Batteries

Suppressing Universal Cathode Crossover in High-Energy Lithium Metal Batteries via a Versatile Interlayer Design**

Chuyi Xie[+], Chen Zhao[+], Heonjae Jeong, Tianyi Li, Luxi Li, Wenqian Xu, Zhenzhen Yang, Cong Lin, Qiang Liu, Lei Cheng, Xingkang Huang, Gui-Liang Xu, Khalil Amine,* and Guohua Chen**

Abstract: The universal cathode crossover such as chemical and oxygen has been significantly overlooked in lithium metal batteries using high-energy cathodes which leads to severe capacity degradation and raises serious safety concerns. Herein, a versatile and thin (≈25 μm) interlayer composed of multifunctional active sites was developed to simultaneously regulate the Li deposition process and suppress the cathode crossover. The as-induced dual-gradient solid-electrolyte interphase combined with abundant lithiophilic sites enable stable Li stripping/plating process even under high current density of 10 mA cm^{-2}. Moreover, X-ray photoelectron spectroscopy and synchrotron X-ray experiments revealed that N-rich framework and CoZn dual active sites can effectively mitigate the undesired cathode crossover, hence significantly minimizing Li corrosion. Therefore, assembled lithium metal cells using various high-energy cathode materials including $LiNi_{0.7}Mn_{0.2}Co_{0.1}O_2$, $Li_{1.2}Co_{0.1}Mn_{0.55}Ni_{0.15}O_2$, and sulfur demonstrate significantly improved cycling stability with high cathode loading.

Introduction

The ever-expanding global electric vehicle (EV) market and the pursuit of the long driving range have greatly pushed forward the research and development of high energy-density battery systems. Due to the high specific capacity (3860 mAh g^{-1}) and low potential (−3.04 V vs. standard hydrogen electrode) of lithium metal anode (LMA),[1] lithium metal batteries (LMBs) coupling with various high-energy cathodes, such as Ni-rich-layered oxides ($Li-Ni_xMn_yCo_zO_2$ Ni-rich NMC),[2] Li-and Mn-rich (LMR) cathode,[3] and sulfur cathode[4] have received great attention. However, the poor stripping/plating behavior of LMA would result in the formation of deadly dendritic Li[5] and hence deteriorate the cycle life, significantly hindering the practical application of LMBs.

[*] C. Xie,[+] C. Lin, Dr. Q. Liu, Prof. G. Chen
Department of Mechanical Engineering and Research Institute for Smart Energy (RISE), The Hong Kong Polytechnic University
11 Yuk Choi Rd, Hung Hom (Hong Kong)
E-mail: ghchen1963@gmail.com

Dr. C. Zhao,[+] Dr. Z. Yang, Dr. X. Huang, Dr. G.-L. Xu, Dr. K. Amine
Chemical Sciences and Engineering Division,
Argonne National Laboratory
9700 S Cass Ave, Lemont, IL 60439 (USA)
E-mail: xug@anl.gov
amine@anl.gov

Dr. H. Jeong, Dr. L. Cheng
Materials Science Division, Argonne National Laboratory
9700 S Cass Ave, Lemont, IL 60439 (USA)

Dr. T. Li, Dr. L. Li, Dr. W. Xu
X-ray Sciences Division, Argonne National Laboratory
9700 S Cass Ave, Lemont, IL 60439 (USA)

Dr. K. Amine
Materials Science and Engineering, Stanford University
Stanford, CA 94305 (USA)
and
Materials Science and Nanoengineering,
Mohammed VI Polytechnic University
Lot 660 Hay Moulay Rachid, Ben Guerir 43150 (Morocco)
and
Institute for Research& Medical Consultations,
Imam Abdulrahman Bin Faisal University (IAU)
Dammam (Saudi Arabia)

Prof. G. Chen
School of Energy and Environment,
City University of Hong Kong
Kowloon (Hong Kong)

[+] These authors contributed equally to this work.

[**] The submitted manuscript has been created by UChicago Argonne, LLC, Operator of Argonne National Laboratory ("Argonne"). Argonne, a U.S. Department of Energy Office of Science laboratory, is operated under Contract No. DE-AC02-06CH11357. The Government retains for itself, and others acting on its behalf, a paid-up nonexclusive, irrevocable worldwide license in said article to reproduce, prepare derivative works, distribute copies to the public, and perform publicly and display publicly, by or on behalf of the Government. The Department of Energy will provide public access to these results of federally sponsored research in accordance with the DOE Public Access Plan. http://energy.gov/downloads/doe-public-access-plan

Constructing a protective interlayer with abundant lithiophilic sites to decrease the Li nucleation barrier and regulate the uneven Li^+ flux has shown as an efficient way to improve the Li stripping/plating behavior and thus mitigate the Li dendrite issue.[6–8] Prior work by Cui et al. has revealed that the heterogeneous Li nucleation barrier plays a key role in determining the Li deposition behavior, and dendritic Li will form on the substrate surface with a large nucleation barrier, such as Cu, while film-like Li deposition will take place on the substrate with negligible nucleation barrier, such as Au, Ag, Zn, Co, etc.[5,9,10] This valuable guideline has stimulated the development of numerous interlayers to improve the stability of LMA, such as lithiophilic covalent organic framework,[11] lithiophilic polymer film,[12] and lithiophilic sites decorated rGO/CNF.[6,7,13] However, most of these reported interlayer approaches have been only validated in the cells containing low-capacity $LiFePO_4$ cathode, which did not maximize the high-energy density of LMA.[14–17] Moreover, the severe Li corrosion due to the uncontrollable cathode crossover from other high-energy cathodes (Figure 1a) has been often overlooked in previous LMA interlayers design,[15,18,19] leading to insufficient cycle stability and unsatisfied safety in the reported lithium metal batteries (Supporting Information Table S1).

One of the critical cathode crossovers is caused by the severe cathode dissolution species (CDS). When coupling with high-energy cathodes, such as Ni-rich NMC and LMR cathode, the dissolved transition metal (TM) ions would migrate and direct deposit on the surface of LMA,[20,21] leading to thickening of solid-electrolyte interphase (SEI) and thus dramatically raising the cell impedance.[22] In addition, the uneven deposition of TM-ions will also alter the distribution of Li^+ on the surface of LMA, aggravating the formation of deadly dendritic Li.[23–25] In the case of S cathode, the S redox involves the formation of a series of highly soluble lithium polysulfides (LiPSs) Li_2S_x ($x=4$–8) intermediates during cycling in the common dimethoxyethane (DME)/dioxolane (DOL) electrolyte.[26–28] Thus, the flooding of LiPSs will lead to the well-known LiPSs shuttle, resulting in severe lithium corrosion and hence severe capacity loss and poor energy efficiency in the Li-S cells.[29–31] Another critical cathode crossover issue comes from the oxygen loss from the layered oxide cathodes, which will lead to the accumulation of gaseous O_2 inside the cell.[32] The cathode-released O_2 gas would diffuse to the anode side, and react with lithiated graphite or lithium dendrite in accompany with huge heat generation, thus deteriorating the cycling stability and cell safety.[33] Such O_2 crossover can even occur in solid-state batteries using solid electrolytes, raising serious concerns about battery safety.[34–36] The aforementioned chemical and oxygen crossover from the cathode will dramatically reduce the LMB cycling stability and cause severe safety concerns, which however have been paid less attention.

In this work, we develop a free-standing, versatile and thin (25 μm) interlayer with multifunctional adsorption sites (Figure 1a) to simultaneously regulate the Li stripping/plating behavior and address the aforementioned universal cathode crossover. The high Li^+ affinity of the N-rich core part and the wide-spread CoZn dual active sites within a unique yolk-shell framework in the proposed interlayer can effectively regulate the Li deposition even under high areal capacity (3.0 mAh cm^{-2}) and high current densities (up to 10.0 mA cm^{-2}). More importantly, the strong binding ability of CoZn dual active sites and the N-rich framework can significantly suppress the detrimental chemical crossover during the long-term cycling of high-energy layered oxides and sulfur cathodes, which has been consistently verified by X-ray photoelectron spectroscopy and synchrotron X-ray probes. As a result, with the protection of the CoZn yolk-shell interlayer (CoZn-YSIL), the Li||NMC cell delivers a high capacity retention rate of 87.25 % for 230 cycles, and the Li||S cell can deliver a high areal capacity of 5.32 mAh cm^{-2} after 100 cycles.

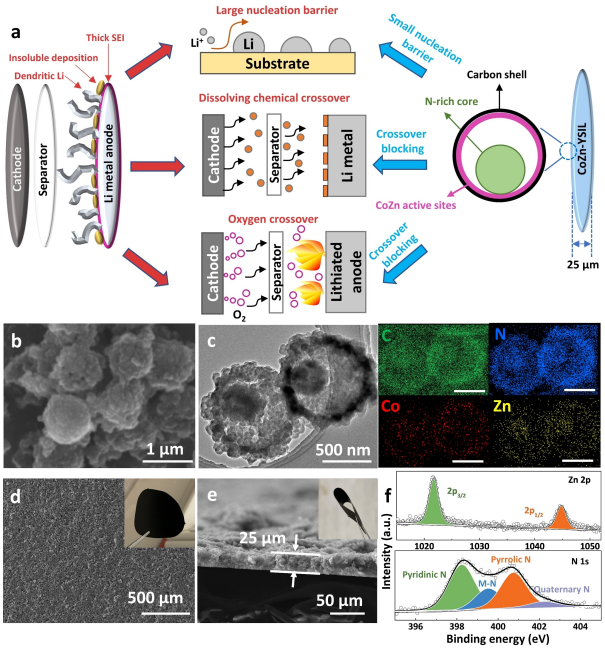

Figure 1. a) Schematic of working principles of CoZn-YSIL in regulating the Li deposition behavior and preventing the Li side reaction with cathode dissolving species and cathode-released O_2. b) SEM image of CoZn-YSs. c) TEM image and corresponding EDS element mappings of CoZn-YSs (interesting elements are C, N, Co, and Zn). d) Top-view SEM image of CoZn-YSIL (inset: digital photograph of CoZn-YSIL). e) Cross section-view SEM image of CoZn-YSIL (inset: digital photograph of folded CoZn-YSIL). f) High-resolution Zn 2p and N 1s XPS spectra of CoZn-YSIL.

Results and Discussion

The detailed synthesis schematic of the preparation process of CoZn-YSIL can be found in Figure S1. As characterized by scanning electron microscopy (SEM), the CoZn yolk-shell spheres (CoZn-YSs) can well maintain their spherical morphology after multilayer coating (Figure S2) and heat treatment, and the size of the as-prepared CoZn-YSs is measured to be ≈1.0 μm (Figure 1b). In addition, the X-ray

diffraction (XRD) results (Figure S3) confirm the successful coating of CoZn-zeolitic imidazolate framework (ZIF) on the surface of melamine-formaldehyde (MF). Due to the uniform dispersion of Co inside the CoZn-ZIF through the crystallization process, the long distance between adjacent Co atom can effectively avoid the aggregate, forming the atomically distributed Co–N–C single-atom site during calcination process.[37] And further coating of resorcinol formaldehyde (RF) resin will not affect the previous ZIF coating layer. To confirm the successful construction of the yolk-shell structure, as well as the introduction of an N-rich core and widespread lithiophilic sites, transmission electron microscopy (TEM) and the corresponding energy dispersive spectroscopy (EDS), were further conducted. As shown in Figure 1c, a typical yolk-shell structure with a ≈400 nm diameter core part and a ≈100 nm thick shell structure can be clearly identified. Moreover, as shown in the corresponding EDS results (Figure 1c), an N-containing framework was successfully constructed, which can improve the Li^+ affinity of the yolk-shell sphere. Meanwhile, the widespread ZnCo active sites inside the yolk-shell spheres can effectively lower the Li nucleation overpotential and enhance the Li deposition inside the yolk-shell spheres.

After the rolling-pressing process, the free-standing thin film CoZn-YSIL can be successfully fabricated. As shown in the top-view SEM image of CoZn-YSIL (Figure 1d), the as-fabricated CoZn-YSIL exhibited continuous and uniform surface features. In addition, as shown in the cross-section SEM image and the digital photograph of the CoZn-YSIL (Figure 1e), the CoZn-YSIL demonstrated good mechanical strength, which did not crack after repeat folding (Figure S4). The thickness of the interlayer is only 25 μm, which is comparable with the commercial Celgard separator. To further confirm the existence of elementary Zn and N-containing lithiophilic sites inside the CoZn-YSIL, X-ray photoelectron spectroscopy (XPS) characterization was conducted. As shown in Figure 1f, the Zn $2p_{3/2}$ (1021.7 eV) and $2p_{1/2}$ (1044.8 eV) can be identified, which agrees well with previously reported elementary Zn XPS results,[38] confirming the existence of elementary Zn. As shown in Figure S5, the peaks of Co $2p_{1/2}$ and Co $2p_{3/2}$ can be identified, and the Co $2p_{3/2}$ peak can be subdivided into three peaks which belong to Co^{3+}(780.6 eV), Co^{2+} (782.4 eV), and satellite peak (786.1 eV),[39] confirming the existence of the Co. Moreover, the N 1s spectrum was deconvoluted into four peaks at 398.2 eV, 399.5 eV, 400.7 eV, and 402.2 eV, which can be assigned to pyridinic-N, metal-N, pyrrolic-N, and quaternary-N, respectively. As revealed by previous work, the pyridinic-N, and pyrrolic-N exhibit high Li^+ affinity.[40,41] Moreover, due to the strong oxygen adsorption energy of CoZn active sites[42,43] and N-rich framework,[44] the cathode-released O_2 crossover issue can also be well addressed.

To validate the benefits of CoZn-YSIL in lowering the Li nucleation barrier and stabilizing the Li stripping/plating process, Li-Cu cells with and without the CoZn-YSIL were tested in common carbonate (Gen II) electrolyte. As shown in Figure 2a, because of the large thermodynamic mismatch between Li and Cu, there was a huge overpotential of

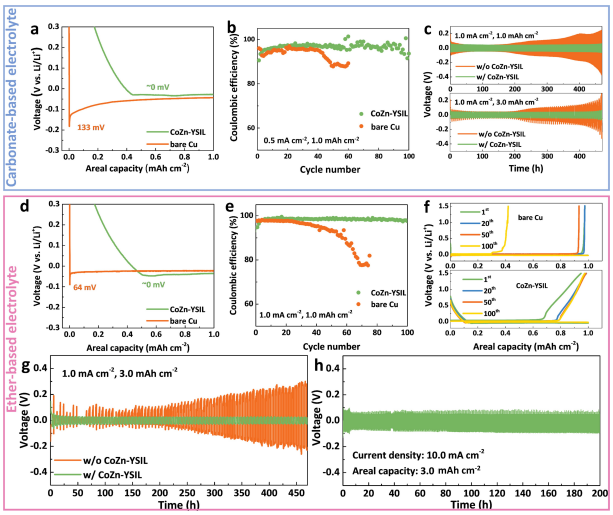

Figure 2. a) Voltage profiles of galvanostatic Li deposition on bare Cu foil and CoZn-YSIL in carbonate-based electrolyte. b) Long-term cycling performance of Li-Cu cells with and without CoZn-YSIL in carbonate-based electrolyte (0.5 mA cm^{-2}, 1.0 mAh cm^{-2}). c) Long-term Li||Li symmetrical cells with and without CoZn-YSIL in carbonate-based electrolyte under different testing conditions (up: 1.0 mA cm^{-2}, 1.0 mAh cm^{-2}; down: 1.0 mA cm^{-2}, 3.0 mAh cm^{-2}). d) Voltage profiles of galvanostatic Li deposition on bare Cu foil and CoZn-YSIL in ether-based electrolyte at 0.5 mA cm^{-2}. e) Long-term Li-Cu cells with and without CoZn-YSIL in ether-based electrolyte under 1.0 mA cm^{-2} and 1.0 mAh cm^{-2}. f) Voltage profiles of various cycles of Li-Cu cells with and without CoZn-YSIL (1.0 mA cm^{-2}, 1.0 mAh cm^{-2}). g) Long-term Li||Li symmetrical cells with and without CoZn-YSIL in ether-based electrolyte (1.0 mA cm^{-2}, 3.0 mAh cm^{-2}). h) Li||Li symmetrical cell under large current density with CoZn-YSIL in ether-based electrolyte (10.0 mA cm^{-2}, 3.0 mAh cm^{-2}).

133 mV under the current density of 0.5 mA cm^{-2} for the bare Cu foil to overcome the heterogeneous nucleation barrier. By contrast, the CoZn-YSIL can effectively eliminate the Li nucleation barrier due to the low Li nucleation overpotential of the CoZn substrate in the CoZn-YSIL. The improved Li affinity of CoZn-YSIL can help to regulate the Li^+ flux and thus improve the Li stripping/plating stability. As shown in Figure 2b, the Li-Cu cell with the existence of CoZn-YSIL can be stably cycled with higher Coulombic efficiency of >97 % within 100 cycles, while the bare Cu can only sustain for 45 cycles with a much lower Coulombic efficiency (<90 %). The long-term cycling stability was further evaluated in symmetric cell tests. As shown in Figure 2c, when the areal capacity was set as 1.0 mAh cm^{-2}, the Li||Li symmetric cell without the CoZn-YSIL can be only cycled for ≈200 h, and the overpotential suddenly increased afterward due to the formation of lithium dendrite. By contrast, the Li||Li symmetric cell with two pieces of CoZn-YSIL on both sides of the separator can be stably cycled for more than 450 h with a small overpotential of ≈45 mV (Figure S6a). Moreover, when we further increased the areal capacity to 3.0 mAh cm^{-2}, the symmetric cell without CoZn-YSIL can be only cycled for ≈200 h while the cell with CoZn-YSIL can be still stably cycled for >450 h with a small overpotential of ≈40 mV (Figure S6b),

further confirming the excellent Li stripping/plating stability even under high areal capacity.

To evaluate the capability of CoZn-YSIL in the ether-based electrolyte, similar Li-Cu and Li||Li symmetric cell tests were carried out in the common DME/DOL electrolyte. As shown in Figure 2d, in the ether-based electrolyte, the CoZn-YSIL can also effectively eliminate the Li nucleation overpotential and thus regulate the Li^+ flux to achieve a uniform Li stripping/plating process. In addition, as shown in Figure 2e and f, under the current density of 1.0 mA cm^{-2}, the bare Cu can be only cycled for less than 40 cycles while the cell with CoZn-YSIL can stably cycle for 100 cycles with the Coulombic efficiency >98.5 %. The excellent Li stripping/plating reversibility and stability enabled by the CoZn-YSIL represent an advance compared to most reported LMA protection strategies (Supporting Information Table S2 and Supporting Information Table S3). Meanwhile, the voltage profiles (Figure 2f and Figure S7) of the Li-Cu cell with CoZn-YSIL exhibited a small amount of (de)lithiation capacity (≈0.2 mAh cm^{-2}), which corresponding to Li^+ intercalation into the graphitic carbon[45] and the (de)alloy process of Li-Zn[46] (Figure S8). The reversibility of that part of (de)lithiation capacity was tested through controlling the testing capacity (Figure S9), and the existence of graphitic carbon and Li-Zn buffer layer can further validate the effectiveness of CoZn-YSIL in decreasing the Li nucleation barrier and regulating the stripping/plating behavior. The Li||Li symmetric cell tests were further carried out with a high areal capacity of 3.0 mAh cm^{-2} under 1.0 mA cm^{-2}. As shown in Figure 2g, the Li||Li symmetric cell without the CoZn-YSIL exhibited a fast failure. By contrast, the cell with CoZn-YSIL demonstrated stable cycle stability for up to 450 h with a much smaller overpotential of ≈25 mV (Figure S10). To evaluate the fast-charging LMBs application with CoZn-YSIL, the Li||Li symmetric cell with CoZn-YSIL under the areal capacity of 3.0 mAh cm^{-2} and a large current density of 10.0 mA cm^{-2} was further tested. As shown in Figure 2h, the symmetric cell can deliver a stable cycling performance for over 200 hours with a small overpotential of ≈65 mV.

To visualize the Li deposition morphology and gain insights into the effectiveness of CoZn-YSIL in stabilizing the Li stripping/plating process, SEM characterizations of Li deposited electrodes with various capacities ranging from 0.5 to 3.0 mAh cm^{-2} were carried out. Due to the large heterogeneous nucleation barrier of Cu foil, the Li^+ tends to be unevenly deposited on the surface of bare Cu foil, resulting in the formation of dendritic Li. As shown in Figure 3a and Figure S11, even under a low deposition capacity condition (0.5 mAh cm^{-2}) and a low current density of 0.5 mA cm^{-2}, Li dendrites can be clearly identified on the surface of bare Cu foil. When the deposition capacities were further increased to 1.0, 2.0, and 3.0 mAh cm^{-2}, the Li dendrites became longer and larger (top panels of Figure 3b–d and Figure S11). Moreover, as shown in the cross-section SEM images (bottom panels of Figure 3b–d), along with the increase of the deposition capacity from 1.0 mAh cm^{-2} to 3.0 mAh cm^{-2}, the depositing thickness of the lithium layer also increased from ≈8 μm to ≈40 μm.

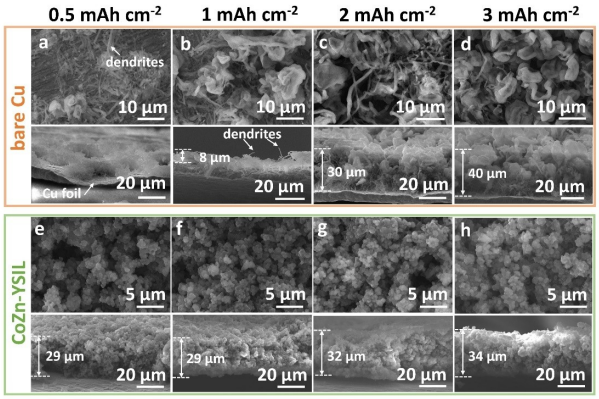

Figure 3. Top-view and cross section-view SEM images of Li-deposited (a–d) bare Cu foil; e)–h) CoZn-YSIL. The Li depositing areal capacity ranging from 0.5–3.0 mAh cm^{-2}, and the current density is 0.5 mA cm^{-2}. Top and bottom panels in (a–d) and (e–h) correspond to front and cross-section view.

The large volume change of Li metal on the surface of Cu foil will also dramatically limit the LMBs performance and cause severe safety concerns. By sharp contrast, with the existence of CoZn-YSIL, no obvious Li dendrite can be found on the electrode surface even under the 3.0 mAh cm^{-2} depositing capacity condition (Figure 3e–h and Figure S12). In addition, the thickness of CoZn-YSIL under various deposition capacities (0.5–3.0 mAh cm^{-2}) did not change too much compared with the pristine CoZn-YSIL (Figure S13), indicating that the continuous Li stripping/plating occurred inside the CoZn-YSIL and the volume change issue of Li metal can also be well addressed by using the CoZn-YSIL to enhance the cell stability and safety. We also characterized the Li deposition morphology under relatively mild current density condition (0.1 mA cm^{-2}). As shown in Figure S14, even under low current density depositing condition, Li dendrite can still be clearly identified on the surface of bare Cu after deposition. By contrast, due to the regulated Li stripping/plating behavior by the CoZn-YSIL, the Li dendrite cannot be found on the surface of CoZn-YSIL (Supporting Information Figure S15).

The effectiveness of CoZn-YSIL in improving the stability of LMB when coupling with the cathodes with limited crossover issue, such as $LiFePO_4$ (LFP) cathode, was evaluated (Figure S16 and S17), and the Li||LFP cell can deliver a high capacity retention rate of 91.9 % for 100 cycles even under a high areal loading of 12.4 mg cm^{-2}. Considering that the next-generation high-capacity cathodes (Ni-rich NMC, LMR, and sulfur) are suffering from the dissolution issue and the flooding CDS will cause severe side reactions with LMA, we further evaluated the effectiveness of CoZn-YSIL in stabilizing the LMBs using high capacity cathodes with severe dissolution issue. We firstly chose $LiNi_{0.7}Mn_{0.2}Co_{0.1}O_2$ NMC cathode as an example because the Ni-rich NMC cathode can deliver a high discharge voltage and capacity but suffer from transition metal dissolution issues. As shown in Figure 4a and b, the Li||NMC cell without CoZn-YSIL can deliver an initial

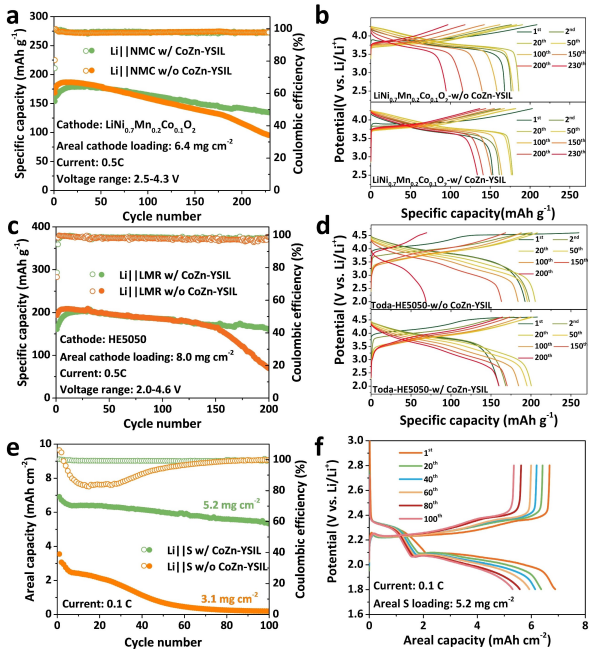

Figure 4. a) Cycling performance of Li||NMC cells with and without CoZn-YSIL under the current of 0.5 C. b) Charge and discharge voltage profiles of various cycles of Li||NMC cells with and without CoZn-YSIL under the current of 0.5 C. c) Cycling performance of Li||LMR cells with and without CoZn-YSIL under the current of 0.5 C. d) Charge and discharge voltage profiles of various cycles of Li||LMR cells with and without CoZn-YSIL under the current of 0.5 C. e) Cycling performance of high-loading Li||S cells with and without CoZn-YSIL at the cathode side under the current of 0.1 C. f) Charge and discharge voltage profiles of various cycles of high-loading Li-S cell with CoZn-YSIL under the current of 0.1 C.

capacity of 168.5 mAh g^{-1}, but can only maintain a capacity of 94.9 mAh g^{-1} after 230 cycles, corresponding to a capacity retention rate of 56.32 %. By contrast, due to the binding ability of CoZn-YSIL toward the dissolved TM species, the cycling stability of Li||NMC cell with CoZn-YSIL was greatly enhanced, which can deliver a high capacity retention rate of 87.25 % after 230 cycles. We further investigate the capability of CoZn-YSIL in stabilizing LMBs coupling with $Li_{1.2}Co_{0.1}Mn_{0.55}Ni_{0.15}O_2$ (TODA HE5050) because of the even severe TM dissolution issue and higher specific capacity of the LMR cathode than conventional NMC cathodes. As shown in Figure 4c and d, the Li||LMR without CoZn-YSIL can only maintain a specific capacity of 68.9 mAh g^{-1} after 200 cycles at 0.5 C, corresponding to a capacity retention rate of 35.7 %. By contrast, for the Li||LMR cell with CoZn-YSIL, the cell can deliver an initial specific capacity of 160.3 mAh g^{-1} at 0.5 C, and well maintain a reversible specific capacity of 164.7 mAh g^{-1} after 200 cycles. The significantly improved cycling stability indicates that the CoZn-YSIL can effectively prevent the side reactions between the LMA and the dissolved cathode species.

Furthermore, we further carried out a series of tests in Li-S cell, which is known for the severe LiPSs flooding issue. As shown in Figure 4e, due to the severe side reaction between LMA and dissolved LiPSs, the cell areal capacity quickly faded to 0.67 mAh cm^{-2} after only 50 cycles, and it can only maintain an areal capacity of 0.17 mAh cm^{-2} after 100 cycles. Considering that the CoZn active sites can not only provide strong binding capability towards dissolved LiPSs but also catalyze the S cathode electrochemical redox, we then set the CoZn-YSIL at both the cathode and anode sides to evaluate the cell performance with high areal S loading (Figure S18 and Figure S19). As shown in Figure 4e and f, the Li-S cell can deliver a high initial specific capacity of 1327 mAh g^{-1} and areal capacity of 6.90 mAh cm^{-2} at 0.1 C, and can maintain a high areal capacity of 5.32 mAh cm^{-2} after 100 cycles, confirming that the CoZn-YSIL can effectively confine and catalyze the dissolved LiPSs to prevent the side reactions with LMA.

To monitor the phase transformation of Li-S cell with CoZn-YSIL, in situ high-energy X-ray diffraction (HEXRD) characterization was carried out. As shown in Figure 5a, before charge/discharge (t = 0 h), peaks located at 4.00°, 4.14°, 4.29°, 5.26°, 5.69°, 6.03°, 6.52°, 7.57°, 7.74°, 7.89°, 8.02°, and 8.13° can be assigned to the (026), (311), (206), (137), (317), (0210), (319), (2212), (357), (535), (602), and (175) peaks of S_8 respectively (ICSD: 130219). Meanwhile,

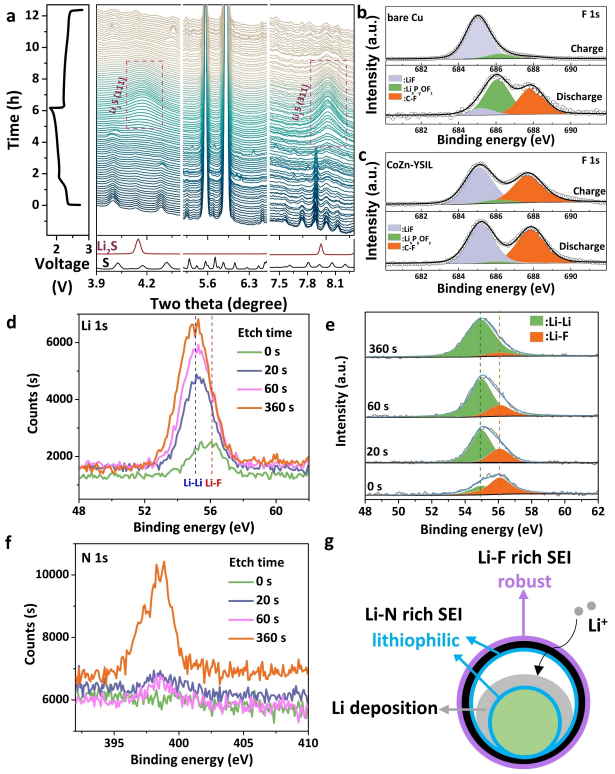

Figure 5. a) In situ HEXRD patterns and the corresponding charge and discharge profiles of Li-S cell with CoZn-YSIL at the cathode side. b) High-resolution F 1s XPS spectra of bare Cu foil at Li stripped and plated states. c) High-resolution F 1s XPS spectra of CoZn-YSIL at Li stripped and plated states. d) Depth-profiling high-resolution N 1s XPS spectra of Li-deposited CoZn-YSIL with the etching time ranging from 0–360 s. e), f) Depth-profiling high-resolution Li 1s XPS spectra of Li-deposited CoZn-YSIL with the etching time ranging from 0–360 s. g) Schematic graph of dual-gradient SEI in CoZn-YSIL.

as the discharge time increased, the peak intensities of the aforementioned S_8 peaks gradually decreased, suggesting the continuous consumption of active material S_8. When the cell voltage reached around 1.95 V ($t \approx 4.7$ h), the S_8 phase completely vanished and the Li_2S phase start to form as the intensities of peaks located at 4.17° and 8.03° began to increase, which can be assigned to the (111) and (311) peaks of Li_2S phase (ICSD: 54396). During the charging process, the peak intensities of Li_2S gradually decreased and fully vanished at the time of ≈10 h. Moreover, at the end of the charged state, the S_8 phase can be identified and no Li_2S can be found, suggesting the thorough oxidization of Li_2S back to S_8. The in situ HEXRD results confirm that the strong binding and catalyzing ability of CoZn-YSIL can effectively improve the cathode active material utilization efficiency and achieve excellent cathode redox reversibility to enable the high electrochemical performance of Li-S batteries.

To gain insight into the CoZn-YSIL in stabilizing LMBs, we further carried out the surface and depth-profiling XPS characterizations of electrodes at different electrochemical stages to analyze the interfacial properties. For the bare Cu electrode, as shown in Figure 5b, the SEI was mainly composed of Li-F species with a small amount of $Li_xP_yOF_z$ species at the charged state. However, at discharged state, the main component of SEI changed to $Li_xP_yOF_z$ and C-F species, and the proportion of Li-F species greatly decreased. The significant change of SEI composition on the bare Cu surface at charged and discharged states indicates that the uneven Li deposition and the large volume change of lithium anode will greatly decrease the stability of SEI, leading to the continuous consumption of electrolyte and the low cell Coulombic efficiency. In the case of CoZn-YSIL, as shown in Figure 5c, the SEI composition and the proportion of each component did not undergo a visible change at charged and discharged states, suggesting that the CoZn-YSIL can enable a stable SEI layer on the electrode surface. To analyze the Li deposition process, depth-profiling XPS characterization of Li-deposited CoZn-YSIL electrode was further conducted. As shown in Figure 5d, the N 1s signal intensity at the outer surface is very weak (0–60 s etching time), while its intensity is gradually increased at the inner part of CoZn-YSIL. Combining with the N 1s XPS fitting results (Figure S20), the content of lithiophilic pyridinic-N is much higher at the inner part of CoZn-YSIL and Li-N bond was also identified at the inner part of the CoZn-YSIL, indicating that the inner part of CoZn-YSIL can effectively adsorb Li^+ and induce the deposition inside the CoZn-YSIL. Moreover, as shown in Figure 5e and f, the intensity of Li-F on the outer surface is higher than the inner part, indicating that a robust Li-F rich SEI was formed on the surface of CoZn-YSIL. In addition, the content of metallic Li-Li on the outer surface was very weak, and it gradually increased as the etching time increased, indicating that most of the Li was deposited inside the CoZn-YSIL. The depth-profiling XPS results further confirm that the CoZn-YSIL can enable the formation of dual-gradient SEI (i.e. Li-F dominates the outer surface while Li-N dominates the inner surface) and regulate the Li deposition inside the CoZn-YSIL to prevent the large volume change during operation and avoid the formation of dendritic Li. As shown in Figure 5g, the formation of robust Li-F rich SEI on the outer surface can effectively improve the structural stability and prevent the formation of dendritic Li due to the relatively high surface energy of Li-F.[47] In addition, the abundant lithophilic sites as well as the Li-N rich SEI at the inner surface can effectively regulate the Li deposition, preventing the large volume change.[48,49]

To provide direct evidence of CoZn-YSIL in addressing the universal cathode crossover issue in LMBs, X-ray fluorescence microscopy (XFM) and XPS characterizations were further carried out. Figure 6a–d exhibit the XFM images of cycled Li metal foils in Li||NMC and Li||S cells after 100 cycles with/without the CoZn-YSIL protection (electrochemical performance can be found in Figure S21). Before conducting the XFM characterizations, the corresponded cycled cells were disassembled, and the CoZn-YSIL was removed from the surface of cycled Li metal foils. In the case of Li||NMC cell without CoZn-YSIL, the absence of CoZn-YSIL (Figure 6a) will lead to the direct deposition of dissolved TM ions on the surface of cycled

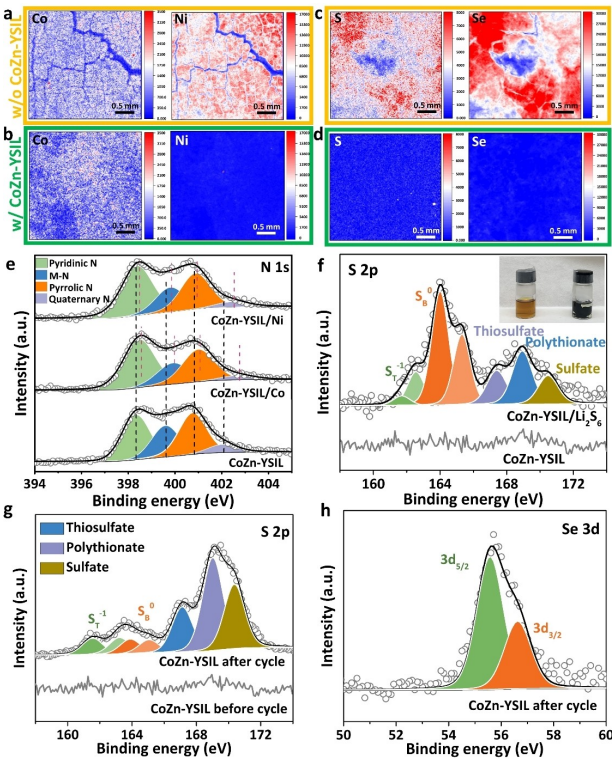

Figure 6. X-ray fluorescence microscopy (XFM) images of Co/Ni and S/Se on the cycled Li metal foils in (a, b) Li||NMC cell and (c, d) Li||S cell with and without the CoZn-YSIL, respectively. The color bar indicates the signal intensity changing from blue (low) to red (high). e) High-resolution N 1s XPS spectra of CoZn-YSIL before and after soaking in 5 mM Ni^{2+} and 5 mM Co^{2+} solutions for 24 h. f) High-resolution S 2p XPS spectra of CoZn-YSIL before and after soaking in 5 mM Li_2S_6 solution for 24 h (inset: digital photograph of 5 mM Li_2S_6 solution with CoZn-YSIL (left) and without CoZn-YSIL (right) after 24 h). g) High-resolution S 2p XPS and h) Se 3d XPS spectra of CoZn-YSIL before and after cycling in Li||S cell for 100 cycles.

LMA as strong and non-uniform Ni and Co signals have been detected on the surface of cycled LMA, decreasing the Li stripping/plating uniformity and increasing the cell internal resistance (Figure S22). By sharp contrast, after applying the CoZn-YSIL, the intensity of Ni and Co signals was greatly decreased (Figure 6b), confirming the effective prevention of TM ions crossover in the cycled Li||NMC cell. For the Li||S cell without the CoZn-YSIL, due to the severe polysulfide/polyselenide shuttle effect, strong S and Se signals can be identified on the surface of cycled LMA (Figure 6c). Nevertheless, the strong binding ability of CoZn-YSIL can greatly suppress the Li corrosion caused by the side reaction between LMA and dissolved polysulfide/polyselenide as the S and Se signals are much lower on the surface of cycled LMA (Figure 6d).

To further investigate the effectiveness of CoZn-YSIL in enhancing the Li affinity as well as preventing the O_2 crossover. First-principles density functional theory (DFT) simulations were carried out. The calculation details can be found in Supporting Information, and We optimized the three different slabs, such as pure graphene, graphene doped with N and Co atoms, and graphene with Zn. Figures S23b–d shows the optimized geometries. We simulate the binding energies of Li and O_2 on these different slabs. The binding energies of Li (and O_2) are computed as $E_{slab+Li\ (O_2)}-E_{slab}-E_{Li\ (O_2)}$. Due to O_2 and Co atom in the graphene slab, we performed spin polarized simulations. Figures S23e–j show the optimized geometries of Li and O_2 with graphene, graphene doped with N and Co atoms, and graphene with Zn, respectively. The DFT simulations show the binding energies of Li atom on graphene, graphene doped with N and Co atoms, and graphene with Zn is −1.57, −2.94, and −1.77 eV. For the binding energies of O_2 on graphene, graphene doped with N and Co atoms, and graphene with Zn is −0.14, −0.91, and −0.16 eV. Compared to the pure graphene, graphene doped with N and Co atoms and graphene with Zn entails the higher binding strength, confirming the improvement of Li affinity and O_2 adsorption through the introduction of CoZn-YSIL.

The binding features of CoZn-YSIL toward dissolved TM ions and polysulfide were further investigated through XPS characterizations. After immersing the CoZn-YSIL into 5 mM Ni^{2+} (CoZn-YSIL/Ni), 5 mM Co^{2+} (CoZn-YSIL/Co), and 5 mM Mn^{2+} (CoZn-YSIL/Mn) solutions for 24 h, TM ions' 2p peaks can be identified on the surface of CoZn-YSIL (Figure S24), suggesting the strong binding ability of CoZn-YSIL to the dissolved TM ions. Moreover, the peaks of pyridinic-N and pyrrolic-N shifted ≈0.2 eV to higher binding energy (Figure 6e), which indicates the electron transfer from the N to the TM ions,[50] confirming the binding ability of pyridinic-N and pyrrolic-N toward dissolved TM ions. Meanwhile, after soaking the CoZn-YSIL in 5 mM Li_2S_6 solution for 24 hours, the solution changed from brown to colorless (Figure 6f), suggesting the strong binding ability of CoZn-YSIL toward LiPSs. Moreover, the XPS result of the soaked sample (Figure 6f) exhibits a strong polysulfide signal on the surface of CoZn-YSIL, indicating the effective binding ability of CoZn-YSIL toward dissolved LiPSs. In addition, S and Se signals were also detected on the surface of cycled CoZn-YSIL (Figure 6g and h), further confirming that the CoZn-YSIL can effectively prevent the Li corrosion caused by the side reaction between LMA and dissolved CDS.

Conclusion

In summary, we have developed a thin (25 μm) interlayer membrane with high Li^+ affinity and multifunctional adsorption ability to enhance the cycling stability of LMB by regulating the Li stripping/plating process and suppressing the universal cathode crossover all-in-one-stroke. The low Li nucleation overpotential of CoZn dual active sites, combined with the N-rich yolk-shell structure, can effectively regulate the Li^+ flux and improve the Li stripping/plating stability. More importantly, the strong binding ability of the CoZn-YSIL can well address the severe cathode crossover issue, preventing the Li side reaction with CDS and cathode-released O_2 when coupling with the high-energy cathodes, such as layered metal oxide NMC, LMR, and S cathodes. As a result, with the protection of CoZn-YSIL, the cycling stability of LMB using various high-capacity cathodes have been significantly improved. In addition, a series of interphase studies as well as in situ HEXRD were carried out to gain insights into the effectiveness of CoZn-YSIL in stabilizing LMB. Our results highlight the importance of interlayer structure design in improving the cell performance of LMB by overcoming the critical cathode crossover.

Acknowledgements

Research at the Hong Kong Polytechnic University was funded by research grants from Shenzhen Science and Technology Program (SGDX20190816230615451), the Guangdong Basic and Applied Basic Research Foundation (No. 2020A1515110798), GDSTC-Guangdong-HK-Macao Joint Laboratory for Photonic-Thermal-Electrical Energy Materials and Devices (GDSTC No. 2019B121205001). Research at the Argonne National Laboratory was funded by the US Department of Energy (DOE), Vehicle Technologies Office. Support from Tien Duong of the US DOE's Office of Vehicle Technologies Program is gratefully acknowledged. Use of the Advanced Photon Source (APS), an Office of Science user facilities, was supported by the US Department of Energy, Office of Science and Office of Basic Energy Sciences, under contract no. DE-AC02-06CH11357. G.X. and K.A. thank the Clean Vehicle Consortium, US, China Clean Energy Research Centre (CERC-CVC2) for support.

Conflict of Interest

The authors declare no conflict of interest.

Data Availability Statement

The data that support the findings of this study are available from the corresponding author upon reasonable request.

Keywords: Cathode Cross-over · High-Energy Cathode · Lithium-Metal Batteries · Solid-Electrolyte Interphase

[1] J. Liu, Z. Bao, Y. Cui, E. J. Dufek, J. B. Goodenough, P. Khalifah, Q. Li, B. Y. Liaw, P. Liu, A. Manthiram, Y. S. Meng, V. R. Subramanian, M. F. Toney, V. V. Viswanathan, M. S. Whittingham, J. Xiao, W. Xu, J. Yang, X.-Q. Yang, J.-G. Zhang, *Nat. Energy* **2019**, *4*, 180–186.

[2] C. Xu, K. Märker, J. Lee, A. Mahadevegowda, P. J. Reeves, S. J. Day, M. F. Groh, S. P. Emge, C. Ducati, B. Layla Mehdi, C. C. Tang, C. P. Grey, *Nat. Mater.* **2021**, *20*, 84–92.

[3] T. Liu, J. Liu, L. Li, L. Yu, J. Diao, T. Zhou, S. Li, A. Dai, W. Zhao, S. Xu, Y. Ren, L. Wang, T. Wu, R. Qi, Y. Xiao, J. Zheng, W. Cha, R. Harder, I. Robinson, J. Wen, J. Lu, F. Pan, K. Amine, *Nature* **2022**, *606*, 305–312.

[4] C. Zhao, G.-L. Xu, Z. Yu, L. Zhang, I. Hwang, Y.-X. Mo, Y. Ren, L. Cheng, C.-J. Sun, Y. Ren, X. Zuo, J.-T. Li, S.-G. Sun, K. Amine, T. Zhao, *Nat. Nanotechnol.* **2021**, *16*, 166–173.

[5] K. Yan, Z. Lu, H.-W. Lee, F. Xiong, P.-C. Hsu, Y. Li, J. Zhao, S. Chu, Y. Cui, *Nat. Energy* **2016**, *1*, 16010.

[6] K. H. Han, J. Y. Seok, I. H. Kim, K. Woo, J. H. Kim, G. G. Yang, H. J. Choi, S. Kwon, E. I. Jung, S. O. Kim, *Adv. Mater.* **2022**, *34*, 2203992.

[7] J. Pu, J. Li, Z. Shen, C. Zhong, J. Liu, H. Ma, J. Zhu, H. Zhang, P. V. Braun, *Adv. Funct. Mater.* **2018**, *28*, 1804133.

[8] J. Chen, Z. Li, N. Sun, J. Xu, Q. Li, X. Yao, J. Ming, Z. Peng, *ACS Energy Lett.* **2022**, *7*, 1594–1603.

[9] Z. Guo, F. Wang, Z. Li, Y. Yang, A. G. Tamirat, H. Qi, J. Han, W. Li, L. Wang, S. Feng, *J. Mater. Chem. A* **2018**, *6*, 22096–22105.

[10] R. Jiang, W. Diao, D. Xie, F. Tao, X. Wu, H. Sun, W. Li, J. Zhang, *ACS Appl. Energy Mater.* **2021**, *4*, 12871–12881.

[11] Z. Li, W. Ji, T.-X. Wang, Y. Zhang, Z. Li, X. Ding, B.-H. Han, W. Feng, *ACS Appl. Mater. Interfaces* **2021**, *13*, 22586–22596.

[12] X. Cui, Y. Chu, X. Wang, X. Zhang, Y. Li, Q. Pan, *ACS Appl. Mater. Interfaces* **2021**, *13*, 44983–44990.

[13] Q. Qin, N. Deng, L. Wang, L. Zhang, Y. Jia, Z. Dai, Y. Liu, W. Kang, B. Cheng, *Chem. Eng. J.* **2019**, *360*, 900–911.

[14] H. Chen, Y. Yang, D. T. Boyle, Y. K. Jeong, R. Xu, L. S. de Vasconcelos, Z. Huang, H. Wang, H. Wang, W. Huang, H. Li, J. Wang, H. Gu, R. Matsumoto, K. Motohashi, Y. Nakayama, K. Zhao, Y. Cui, *Nat. Energy* **2021**, *6*, 790–798.

[15] M. Huang, Z. Yao, Q. Yang, C. Li, *Angew. Chem. Int. Ed.* **2021**, *60*, 14040–14050.

[16] Y. Mei, J. Zhou, Y. Hao, X. Hu, J. Lin, Y. Huang, L. Li, C. Feng, F. Wu, R. Chen, *Adv. Funct. Mater.* **2021**, *31*, 2106676.

[17] C. Jin, T. Liu, O. Sheng, M. Li, T. Liu, Y. Yuan, J. Nai, Z. Ju, W. Zhang, Y. Liu, Y. Wang, Z. Lin, J. Lu, X. Tao, *Nat. Energy* **2021**, *6*, 378–387.

[18] Y. Yuan, F. Wu, Y. Bai, Y. Li, G. Chen, Z. Wang, C. Wu, *Energy Storage Mater.* **2019**, *16*, 411–418.

[19] H. Jiang, Y. Zhou, C. Guan, M. Bai, F. Qin, M. Yi, J. Li, B. Hong, Y. Lai, *Small* **2022**, *18*, 2107641.

[20] C. Zhan, J. Lu, A. Jeremy Kropf, T. Wu, A. N. Jansen, Y.-K. Sun, X. Qiu, K. Amine, *Nat. Commun.* **2013**, *4*, 2437.

[21] J. Li, A. Manthiram, *Adv. Energy Mater.* **2019**, *9*, 1902731.

[22] H. Y. Asl, A. Manthiram, *Science* **2020**, *369*, 140–141.

[23] W. Li, *J. Electrochem. Soc.* **2020**, *167*, 090514.

[24] G. Zhou, X. Sun, Q.-H. Li, X. Wang, J.-N. Zhang, W. Yang, X. Yu, R. Xiao, H. Li, *J. Phys. Chem. Lett.* **2020**, *11*, 3051–3057.

[25] T. Li, X.-Z. Yuan, L. Zhang, D. Song, K. Shi, C. Bock, *Electrochem. Energy Rev.* **2020**, *3*, 43–80.

[26] C. Zhao, G.-L. Xu, T. Zhao, K. Amine, *Angew. Chem. Int. Ed.* **2020**, *59*, 17634–17640.

[27] B.-J. Lee, C. Zhao, J.-H. Yu, T.-H. Kang, H.-Y. Park, J. Kang, Y. Jung, X. Liu, T. Li, W. Xu, X.-B. Zuo, G.-L. Xu, K. Amine, J.-S. Yu, *Nat. Commun.* **2022**, *13*, 4629.

[28] G.-L. Xu, H. Sun, C. Luo, L. Estevez, M. Zhuang, H. Gao, R. Amine, H. Wang, X. Zhang, C.-J. Sun, Y. Liu, Y. Ren, S. M. Heald, C. Wang, Z. Chen, K. Amine, *Adv. Energy Mater.* **2019**, *9*, 1802235.

[29] L. Qie, C. Zu, A. Manthiram, *Adv. Energy Mater.* **2016**, *6*, 1502459.

[30] L. Kong, Q. Jin, X.-T. Zhang, B.-Q. Li, J.-X. Chen, W.-C. Zhu, J.-Q. Huang, Q. Zhang, *J. Energy Chem.* **2019**, *39*, 17–22.

[31] S. Jiang, X. Xu, J. Yin, X. Zhu, L. Wei, K. Xi, L. Zhang, Y. Lan, H. Wu, Y. Gao, *J. Power Sources* **2022**, *529*, 231195.

[32] H. Zhang, H. Liu, L. F. J. Piper, M. S. Whittingham, G. Zhou, *Chem. Rev.* **2022**, *122*, 5641–5681.

[33] X. Liu, D. Ren, H. Hsu, X. Feng, G.-L. Xu, M. Zhuang, H. Gao, L. Lu, X. Han, Z. Chu, J. Li, X. He, K. Amine, M. Ouyang, *Joule* **2018**, *2*, 2047–2064.

[34] W. Yu, C. Xue, B. Hu, B. Xu, L. Li, C.-W. Nan, *Energy Storage Mater.* **2020**, *27*, 244–251.

[35] X. Lin, F. Sun, Q. Sun, S. Wang, J. Luo, C. Zhao, X. Yang, Y. Zhao, C. Wang, R. Li, X. Sun, *Chem. Mater.* **2019**, *31*, 9024–9031.

[36] G. Huang, J. Wang, X. Zhang, *ACS Cent. Sci.* **2020**, *6*, 2136–2148.

[37] X. Wang, Z. Chen, X. Zhao, T. Yao, W. Chen, R. You, C. Zhao, G. Wu, J. Wang, W. Huang, *Angew. Chem. Int. Ed.* **2018**, *57*, 1944–1948.

[38] B. Dilasari, Y. Jung, K. Kwon, *J. Ind. Eng. Chem.* **2017**, *45*, 375–379.

[39] J. He, A. Manthiram, *Adv. Energy Mater.* **2020**, *10*, 2002654.

[40] X. Feng, H.-H. Wu, B. Gao, M. Świętosławski, X. He, Q. Zhang, *Nano Res.* **2022**, *15*, 352–360.

[41] R. Zhang, X. R. Chen, X. Chen, X. B. Cheng, X. Q. Zhang, C. Yan, Q. Zhang, *Angew. Chem. Int. Ed.* **2017**, *56*, 7764–7768.

[42] M. Sharma, J.-H. Jang, D. Y. Shin, J. A. Kwon, D.-H. Lim, D. Choi, H. Sung, J. Jang, S.-Y. Lee, K. Y. Lee, H.-Y. Park, N. Jung, S. J. Yoo, *Energy Environ. Sci.* **2019**, *12*, 2200–2211.

[43] J. Zhang, H. Yang, B. Liu, *Adv. Energy Mater.* **2021**, *11*, 2002473.

[44] G.-L. Xu, Q. Liu, K. K. S. Lau, Y. Liu, X. Liu, H. Gao, X. Zhou, M. Zhuang, Y. Ren, J. Li, M. Shao, M. Ouyang, F. Pan, Z. Chen, K. Amine, G. Chen, *Nat. Energy* **2019**, *4*, 484–494.

[45] W. Ye, F. Pei, X. Lan, Y. Cheng, X. Fang, Q. Zhang, N. Zheng, D.-L. Peng, M.-S. Wang, *Adv. Energy Mater.* **2020**, *10*, 1902956.

[46] S. Jin, Y. Ye, Y. Niu, Y. Xu, H. Jin, J. Wang, Z. Sun, A. Cao, X. Wu, Y. Luo, H. Ji, L.-J. Wan, *J. Am. Chem. Soc.* **2020**, *142*, 8818–8826.

[47] Z. Wang, Z. Sun, J. Li, Y. Shi, C. Sun, B. An, H.-M. Cheng, F. Li, *Chem. Soc. Rev.* **2021**, *50*, 3178–3210.

[48] Z. Wang, Y. Wang, Z. Zhang, X. Chen, W. Lie, Y.-B. He, Z. Zhou, G. Xia, Z. Guo, *Adv. Funct. Mater.* **2020**, *30*, 2002414.

[49] Q. Dong, B. Hong, H. Fan, H. Jiang, K. Zhang, Y. Lai, *ACS Appl. Mater. Interfaces* **2020**, *12*, 627–636.

[50] J. Yang, W. Li, D. Wang, Y. Li, *Adv. Mater.* **2020**, *32*, 2003300.

Manuscript received: November 27, 2022
Accepted manuscript online: March 14, 2023
Version of record online: April 3, 2023